Benchmark of Models Commonly Used To Simulate Laser-Induced Incandescence of Soot

Romain Lemaire[1], Sébastien Menanteau[2],
[1]TFT Laboratory, Department of Mechanical Engineering, École de technologie supérieure
Montreal, Quebec, H3C 1K3, Canada
romain.lemaire@etsmtl.ca
[2]Energy, Environment & Materials Engineering, Icam Lille, 59016, France
sebastien.menanteau@icam.fr

Abstract – This paper compares the predictive ability of 4 models designed to simulate the laser-induced incandescence of soot. To that end, we considered 2 standard models integrating terms representing heating by absorption of laser energy and cooling by radiation, sublimation and conduction, together with two refined ones, which include mechanisms accounting for soot annealing and oxidation, saturation of linear, single- and multi-photon absorption processes, and cooling by thermionic emission. Predictions by these models were compared with signals measured in an ethylene diffusion flame. Sensitivity analyses focusing on the key parameters influencing the LII phenomenon were, moreover, conducted. As highlights, this work showed that standard models fail to properly simulate the fluence dependence of LII signals in the high fluence regime. More sophisticated models better reproduce LII fluence curves. Further work is required, however, to properly parameterize refined models to enable them to reproduce LII time decays over a wide range of operating conditions. The identification of parameters of interest, such as those involved in multi-photon absorption and nonthermal photodesorption processes, should help guide future works to be undertaken.

***Keywords*:** Combustion, soot, laser-induced incandescence, modeling, parameterization

1. Introduction

Soot emitted by combustion systems drive climate change through radiative forcing and are associated with adverse health effects [1]. There is therefore a crucial need for fundamental efforts targeting the elucidation of soot formation processes. In this context, in situ diagnostics, such as laser-induced incandescence (LII), are required to detect soot in combustion media. LII involves heating particles to their incandescence temperature by means of a pulsed laser source before collecting the radiation emitted above the flame emission using an adapted detector. While used specifically for soot volume fraction assessment [2], LII has also proven to be useful in inferring soot size by coupling a time-resolved detection approach with LII signal modeling [1]. Properly applying these measurement approaches, however, requires a firm understanding of the physical mechanisms and parameters controlling the laser-induced incandescence of soot.

Since the work by [3], significant effort has been expended on developing theoretical models capable of predicting the radiative emission from laser-heated particles. Their predictive capabilities, however, vary significantly, depending on the nature of the energy fluxes integrated within the energy and mass balance equations accounting for the temporal evolution of the soot temperature and diameter during the laser heating and cooling stages [4]. Efforts must therefore be directed at determining the energy and mass-balance mechanisms that must be considered and how they should be parameterized [1]. In view of the foregoing, the present work aims at comparing the ability of 4 LII models from the literature to simulate a set of LII signals measured in an ethylene diffusion flame [5]. To that end, 2 standard model formulations (drawn from [3] (model 1) and [6] (model 2)) are considered and integrate mechanisms representing heating by absorption of the laser energy and cooling by radiation, sublimation and conduction. Supported by the conclusions from [7] showing the importance of integrating additional mechanisms, 2 refined models developed by Michelsen [4,8] are also considered. The first one (model 3) integrates the above-listed energy fluxes with terms representing soot annealing and oxidation [8]. The second one (model 4) neglects annealing, but includes terms standing for saturation of linear, single- and multi-photon absorption processes and cooling by thermionic emission [4]. Predictions from these simulation tools will be compared with signals from [5]. Sensitivity analyses focusing on key parameters influencing

the LII response will also be carried out. Conclusions will then be drawn, noting that the aim of this work is not to state that some models should be preferred over others, but rather, is to identify the potential strengths of particular models, depending on the targeted applications, while proposing insights into how to properly parameterize them.

2. Methodology
2.1. Experimental database
Experimental data are issued from [5], where an atmospheric ethylene diffusion flame was stabilized on a Santoro burner. Soot was irradiated with the 1064-nm output from an injection-seeded Nd:YAG laser providing spatially homogeneous beams and pulses with a smooth temporal profile. Time-resolved LII signals were recorded using a photomultiplier tube with a bandpass filter centered at 681.8 nm. The spectral characteristics of the detection system provided in [5] were integrated into the calculation procedure (see **section 2.2**) while a temperature of the surrounding gases of 1676 K and a primary particle size of 33 nm were considered as inputs according to [5].

2.2. Description of implemented models
All implemented models are based on the following system of coupled differential equations depicting variations of the internal energy rate (dU_{int}/dt) and mass (dM_p/dt) of soot particles as a function of time:

$$\begin{cases} \frac{dU_{int}}{dt} = \dot{Q}_{abs} - \dot{Q}_{sub} - \dot{Q}_{rad} - \dot{Q}_{cond} + \dot{Q}_{ann} + \dot{Q}_{ox} - \dot{Q}_{th} \\ \frac{dM_p}{dt} = \sum_{i=1}^{i_{tot}} \left(\frac{dM_p}{dt}\right)_{sub,i} + \left(\frac{dM_p}{dt}\right)_{ox} \end{cases} \qquad (1)$$

where t is the time, subscripts 'sub' and 'ox' denote the contributions of the sublimation and oxidation mechanisms to the mass loss, respectively, 'i' stands for the contribution of each vaporized carbon cluster C_i to the particle mass loss, while i_{tot} corresponds to the total number of vaporized carbon clusters.

2.2.1. Internal energy: Eq. (2) is used in each model to express the rate of change of energy stored by soot:

$$\frac{dU_{int}}{dt} = N_p \cdot \frac{\pi}{6} \cdot D_p^3 \cdot \frac{d\,T_p}{dt} \cdot [\rho_s \cdot c_s \cdot (1 - X_a) + \rho_a \cdot c_a \cdot X_a] \qquad (2)$$

where N_p, D_p and T_p respectively represent the number of primary particles per aggregate, the diameter and the temperature, X_a stands for the soot annealed fraction, while ρ and c are the density and heat capacity (subscript 's' and 'a' denoting the unannealed and annealed soot fractions, respectively). Annealing is solely considered in model 3 (X_a being set to 0 otherwise). Constant values are considered for ρ_s and c_s [3] in model 1. For models 2 to 4, the temperature-dependent expressions from [6] (model 2) and [8] (models 3 and 4) are used to compute these properties, except for ρ_s, which is constant in model 2, as detailed in [4].

2.2.2. Absorption: Eq. (3) depicts the rate of energy change by absorption of the laser pulse in models 1 to 3:

$$\dot{Q}_{abs} = N_p \cdot [C_{abs,s} + C_{abs,a}] \cdot \frac{F \cdot q_{exp}(t)}{\int_0^{t_l} q_{exp}(t)dt} \qquad (3)$$

where q_{exp}, t_l, λ_l and F are the normalized irradiance, the pulse duration, the excitation wavelength and the energy density, while $C_{abs,s}$ and $C_{abs,a}$ are the absorption cross-section of unannealed and annealed soot, so that:

$$C_{abs,s} = (1 - X_a) \cdot \frac{\pi^2 \cdot D_p^3}{\lambda_l} \cdot E(m) \quad \text{and} \quad C_{abs,a} = X_a \cdot \frac{\pi^2 \cdot D_p^3}{\lambda_l} \cdot f_a \cdot E_a(m) \qquad (4)$$

where $E(m)$ and $E_a(m)$ (set as detailed in **section 3**) are the refractive index functions of the unannealed and annealed soot, respectively. As for model 4, the expression of the absorption flux (see Eq. (5)) includes terms representing the saturation of linear, single- and multi-photon absorption:

$$\dot{Q}_{abs} = N_p \cdot C_{abs,s} \cdot \frac{f_1 \cdot B_{\lambda 1}}{\int_0^{t_l} q_{exp}(t)dt} \left\{1 - exp\left[-\frac{F \cdot q_{exp}(t)}{B_{\lambda 1}}\right]\right\} + N_p \cdot \sigma_{\lambda n} \cdot \frac{\pi \cdot D_p^3 \cdot N_{ss}}{6} \cdot \frac{B_{\lambda n}^n}{\int_0^{t_l} \left(q_{exp}(t)\right)^n dt} \left\{1 - exp\left[-\left(\frac{F \cdot q_{exp}(t)}{B_{\lambda n}}\right)^n\right]\right\} \qquad (5)$$

where f_1 is an empirical scaling factor for linear absorption, n represents the number of photons to be absorbed to photodesorb C_2 clusters, N_{ss} stands for the density of carbon atoms at the soot surface [4], $B_{\lambda 1}$ and $B_{\lambda n}$ are empirical saturation factors related to single-photon and multi-photon absorption processes, while $\sigma_{\lambda n}$ is the cross-section for removal of C_2 clusters by photodesorption.

2.2.3. Sublimation: When being heated above 4000 K, soot sublimes to produce carbon clusters including C_1 to C_{10} to C_{10} species. In models 1 and 2, the evaporative cooling rate is expressed as follows:

$$\dot{Q}_{sub} = N_p \cdot \frac{-\Delta H_v}{\omega_v} \cdot \frac{dM_p}{dt} \tag{6}$$

where ΔH_v represents the enthalpy of formation of carbon clusters and ω_v denotes their molecular weight. As for the mass lost by sublimation, it is calculated according to Eqs. (7) and (8) for models 1 and 2, respectively:

$$\frac{dM_p}{dt} = -\frac{\pi \cdot D_p{}^2 \cdot w_v \cdot \alpha_M \cdot p_v}{R_p \cdot T_p} \cdot \sqrt{\frac{R_m \cdot T_p}{2 \cdot w_v}} \tag{7}$$

$$\frac{dM_p}{dt} = -\frac{\pi \cdot D_p{}^2 \cdot w_v \cdot \alpha_M \cdot p_v}{R_p \cdot T_p} \cdot \sqrt{\frac{R_m \cdot T_p}{2 \cdot w_v}} \cdot \frac{f \cdot k_p \cdot T_p}{\sqrt{2} \cdot \bar{\sigma} \cdot p_0 \cdot D_p \cdot \alpha_M + f \cdot k_p \cdot T_p} \tag{8}$$

where α_M (0.8 [4,9]) is the mass accommodation coefficient of vaporized carbon clusters, R_p and R_m are the universal gas constants expressed in effective pressure and mass units, respectively [4,6], p_v represents the partial pressure of sublimed carbon species, k_p is the Boltzmann constant, $\bar{\sigma}$ stands for the average molecular cross-section for C_1 to C_7 vaporized clusters, p_0 is the ambient pressure, while f denotes the dimensionless Eucken correction to thermal conductivity of polyatomic gas. Constant values for ΔH_v (7.78×10⁵ J·mol⁻¹) and ω_v (36 g·mol⁻¹) are set in model 1, which only considers C_3 clusters. Alternatively, the enthalpy of formation of carbon clusters and their molecular weight are calculated as proposed in [6] for model 2. As for models 3 and 4, the sublimation rate is expressed as follows:

$$\dot{Q}_{sub} = -N_p \cdot \sum_{i=1}^{i_{tot}} \frac{1}{w_i} \cdot \left(\frac{dM_p}{dt}\right)_{sub,i} \cdot \left[\frac{\Delta H_i \cdot \left(P_{sat}^{C_i} - P_{\lambda s} - P_{diss} - P_{\lambda a}\right) + \Delta H_{\lambda n,s} \cdot P_{\lambda s} + \Delta H_{diss} \cdot P_{diss} + \Delta H_{\lambda n,a} \cdot P_{\lambda a}}{P_{sat}^{C_i}}\right] \tag{9}$$

where w_i (12.011×i g·mol⁻¹) and ΔH_i stand for the molecular weight and enthalpy of formation of each C_i cluster (with i_{tot} set to 10 and 5 for models 3 and 4, respectively), $P_{sat}^{C_i}$ refers to the partial saturation pressure of vaporized clusters C_i, $P_{\lambda s}$ and $P_{\lambda a}$ represent the effective pressures calculated based on the rate of nonthermal photodesorption of C_i clusters from the unannealed and annealed particle fractions, respectively, P_{diss} is the effective pressure issued from the rate of thermal photodesorption from annealed soot, $\Delta H_{\lambda n,s}$ and $\Delta H_{\lambda n,a}$ are the energies required to photodesorb C_i clusters from the unannealed and annealed soot fractions, and ΔH_{diss} is the enthalpy of formation of C_i clusters by thermal sublimation of annealed soot [8,10]. Finally, models 3 and 4 integrate Eq. (10) to compute the mass lost by sublimation independently for each C_i species:

$$\left(\frac{dM_p}{dt}\right)_{sub,i} = \frac{-\pi \cdot D_p{}^2 \cdot w_i \cdot \alpha_i}{R_p \cdot T_p} \cdot U_i \cdot B_i \tag{10}$$

where α_i is the mass accommodation coefficient of C_i clusters, B_i is a parameter representing the influence of diffusive and convective mass and heat transfers during sublimation, while U_i corresponds to the ejection speed of C_i away from the particle surface (see [8,10] for more details regarding the calculation procedure allowing to compute these terms).

2.2.4. Radiation: The radiative emission from laser-heated soot is calculated for each model based on Eq. (11):

$$\dot{Q}_{rad} = 8 \cdot \pi \cdot h \cdot c_l{}^2 \cdot N_p \cdot \int_0^{\lambda_\infty} \frac{C_{abs,s} + C_{abs,a}}{\lambda^5} \cdot \left[\frac{1}{exp\left(h \cdot c / \lambda \cdot k_B \cdot T_p\right) - 1} - \frac{1}{exp\left(h \cdot c / \lambda \cdot k_B \cdot T_g\right) - 1}\right] d\lambda \tag{11}$$

where h is the Planck constant, c_l stands for the speed of light, while k_B represents the Boltzmann constant.

2.2.5. Conduction: The rate of energy loss by conduction is calculated for each model based on Eq. (12) [4]:

$$\dot{Q}_{cond} = N_p \cdot \frac{\pi \cdot D_p^2 \cdot p_0}{R_p \cdot T_g} \cdot \alpha_T \cdot \sqrt{\frac{R_m \cdot T_g}{2 \cdot \pi \cdot \omega_a}} \cdot \left(C_p - \frac{R}{2}\right) \cdot (T_p - T_g) \tag{12}$$

where p_0 is the ambient pressure, T_g represents the temperature of the surrounding gaseous species, R is the universal gas constant expressed in standard unit, ω_a is the average molecular weight of air considered as a surrogate for flame gases, C_p stands for the molar heat capacity of the ambient gases at constant pressure, expressed as a of T_g [4], while α_T is the thermal accommodation coefficient whose value is discussed in **section 3**.

2.2.6. Annealing: When being laser-heated, soot may experience significant structure modifications. Following [8], the rate of energy increase by annealing (embedded in model 3) can be expressed as follows:

$$\dot{Q}_{ann} = N_p \cdot \frac{-\Delta H_{imig} \cdot k_{imig} \cdot N_d - \Delta H_{vmig} \cdot k_{vmig} \cdot N_d}{N_A} \tag{13}$$

with N_A being the number of Avogadro, N_d the number of Frenkel Schottky defects, ΔH_{imig} and ΔH_{vmig} the enthalpy for interstitial and vacancy migrations, respectively, while k_{imig} and k_{vmig} stand for the interstitial and vacancy migration rates (see [8,10] for further details regarding the implementation of the annealing flux).

2.2.7. Oxidation: The oxidation of soot induced by the oxygen molecules available in the surrounding atmosphere is considered in models 3 and 4. To that end, the sub-model formulation from [8] is implemented:

$$\dot{Q}_{ox} = N_p \cdot \frac{\left(\Delta H_{ox} + 2 \cdot \alpha_T \cdot C_p^{CO} \cdot T_p\right)}{2 \cdot \omega_1} \cdot \left(\frac{dM_p}{dt}\right)_{ox} \tag{14}$$

where ΔH_{ox} is the enthalpy of formation of CO (set to -2.215×10^5 J·mol^-1), C_p^{CO} is the heat capacity of CO [8], while $\left(dM_p/dt\right)_{ox}$ is expressed as per Eq. (15), in which $k_{ox,s}$ and $k_{ox,a}$ represent the oxidation rate constants of unannealed and annealed soot, respectively:

$$\left(\frac{dM_p}{dt}\right)_{ox} = \frac{-2 \cdot \pi \cdot D_p^2 \cdot \omega_1 \cdot (k_{ox,s} + k_{ox,a})}{N_A} \tag{15}$$

2.2.8. Thermionic emission: The energy loss associated with the thermal ejection of electrons from heated soot is expressed in model 4 by means of 2 sub-models issued from [4] and [11] (see Eqs. (16) and (17), respectively):

$$\dot{Q}_{th} = N_p \cdot \frac{4 \cdot \phi \cdot m_{el} \cdot \left(\pi \cdot D_p \cdot k_B \cdot T_p\right)^2}{h^3} \cdot exp\left(-\frac{\phi}{k_B \cdot T_p}\right) \tag{16}$$

$$\dot{Q}_{th} = N_p \cdot \frac{4 \cdot (\phi + \Delta\phi) \cdot m_{el} \cdot \left(\pi \cdot D_p \cdot k_B \cdot T_p\right)^2}{h^3} \cdot exp\left[-\frac{(\phi + \Delta\phi)}{k_B \cdot T_p}\right] \tag{17}$$

where ϕ represents a constant work function, m_{el} stands for the mass of an electron and $\Delta\phi$ denotes the increased barrier to further electron emission due to a positive charge buildup (see [10,11]).

2.2.9. Resolution: Eq. (1) is solved by implementing the appropriate equations in each model (see **Table 1**). The variations of T_p and D_p as a function of time are then determined and introduced into a Planck function integrated over the spectral range of the detection system to obtain theoretical LII signals.

Table 1: Summary of equations used in each LII model

	dU_{int}/dt	$\dot{Q}_{abs}$	$\dot{Q}_{sub}$	$\dot{Q}_{rad}$	$\dot{Q}_{cond}$	$\dot{Q}_{ann}$	$\dot{Q}_{ox}$	$\dot{Q}_{th}$
Model 1 (X_a=0)	Eq. (2)	Eq. (3)	Eq. (6)	Eq. (11)	Eq. (12)	-	-	-
Model 2 (X_a=0)	Eq. (2)	Eq. (3)	Eq. (6)	Eq. (11)	Eq. (12)	-	-	-
Model 3	Eq. (2)	Eq. (3)	Eq. (9) - i_tot=10	Eq. (11)	Eq. (12)	Eq. (13)	Eq. (14)	-
Model 4 (X_a=0)	Eq. (2)	Eq. (5)	Eq. (9) - i_tot=5	Eq. (11)	Eq. (12)	-	Eq. (14)	Eq. (16) or (17)

3. Results and Discussion
3.1. Results obtained with standard model formulations (models 1 and 2)
The fluence dependence of the peak LII signal as well as the evolution of the maximal soot temperature as a function of the laser fluence are plotted in **Fig. 1**. Simulated results from the implementation of models 1 and 2 are compared therein with experimental data from [5].
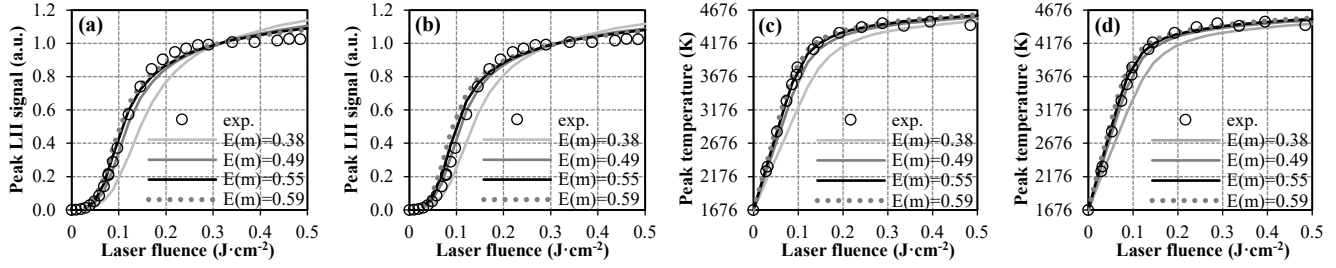
Fig. 1: Comparison of measured (exp.) and simulated LII fluence curves ((a) and (b)) and peak soot temperature profiles as a function of the fluence ((c) and (d)). Calculations are performed with models 1 ((a) and (c)) and 2 ((b) and (d)) with varied $E(m)$.

As can be seen, using the lowest $E(m)$ value (i.e., 0.38) does not allow properly mimicking measured fluence curves and temperature profiles, regardless of the considered model. On the other hand, setting this parameter, which directly drives the absorption flux, to 0.55 for model 1 and 0.49 for model 2, allows obtaining a good agreement between measured and simulated data. While temperature profiles are globally well reproduced for fluence going up to 0.5 J·cm^{-2} (see **Figs. 1(c)** and **1(d)**), calculated fluence curves still diverge from their experimental counterparts for fluences above ~0.3 J·cm^{-2} (see **Figs. 1(a)** and **1(b)**). Nevertheless, results reported in **Fig. 1** show that both models exhibit an overall good predictive ability in the low-to-intermediate fluence range despite the need to set relatively high soot absorption function values (an $E(m)$ of 0.3 ± 0.06 for a visible to near-infrared (IR) wavelength range being indeed more commonly considered in the literature, as mentioned in [**10**]). It is noteworthy that the inability of models 1 and 2 to properly simulate measured data at high fluences (i.e., above the sublimation threshold) is, however, likely to represent a limitation in terms of using these modeling tools to infer soot volume fractions through the processing of measured signals, for instance. Indeed, the underlying reason for the approximate proportionality between peak LII signals and soot-volume fractions relies on the fact that soot particles behave like volume absorbers and emitters. As a consequence, if all the particles reach the maximum signal for the same peak temperature (corresponding to the sublimation point), the peak signal will then correlate with the volume of the particles. This notably explains why high laser fluences (for which pulsed-LII signals appear independent of the laser fluence, as exemplified above 0.3 J·cm^{-2} in **Figs. 1(a)** and **1(b)**), are often used to assess soot volume fractions in combustion media [**1**]. The relatively poor predictive ability of models 1 and 2 to capture the physics at play during LII measurements at high fluences hence tends to prevent them from being used to derive soot-volume fraction estimates based on the analysis of measured signals. On the other hand, it is preferable for particle sizing by time-resolved LII to avoid sublimation, which can significantly reduce the size of the particles. Sublimation especially makes modeling of measured signals more difficult as it induces complex LII time decays, which are generally more difficult to properly fit. As models 1 and 2 reproduce well fluence curves below the sublimation threshold, we therefore tested their ability to reproduce measured LII times decays. To that end, in **Fig. 2** (model 2), we compared measured signals from [**5**] with simulated ones issued from calculations performed using different values of the thermal accommodation coefficient (α_T), which is a key parameter driving the cooling by conduction and thus the signal time decays (data related to model 1 not presented for brevity as they are similar).
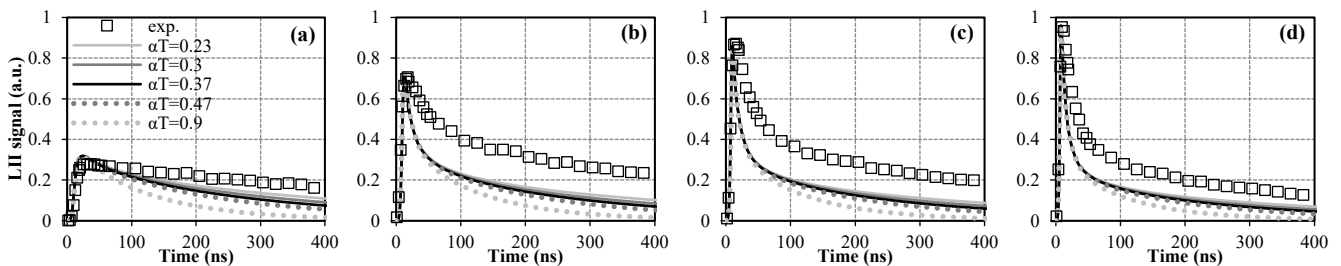

Fig. 2: Comparison of measured and simulated LII time decays for different α_T values. Calculations performed using model 2 with $E(m)$ = 0.49 and fluences of (a) 0.09 J.cm^{-2}, (b) 0.15 J.cm^{-2}, (c) 0.19 J.cm^{-2} and (d) 0.27 J.cm^{-2}.

Obtained results show that tested models do not allow reproducing measured time decays, regardless of the selected α_T. Computed signals indeed always underestimate their experimental counterparts, which means that the models overpredict the soot cooling even when using very low thermal accommodation coefficient values. These observations tend to discard model formulations that are too simplistic from being used to properly simulate LII in the whole fluence range investigated herein. Other experimental datasets should be considered, however, before drawing any clear-cut conclusion, in order to allow determining whether the observed gaps are dependent on the specific experiment or the implemented models.

3.2. Results obtained with refined model formulations (models 3 and 4)

Simulated fluence curves and time decays obtained with model 3 are compared with experimental data from [5] in **Fig. 3**.
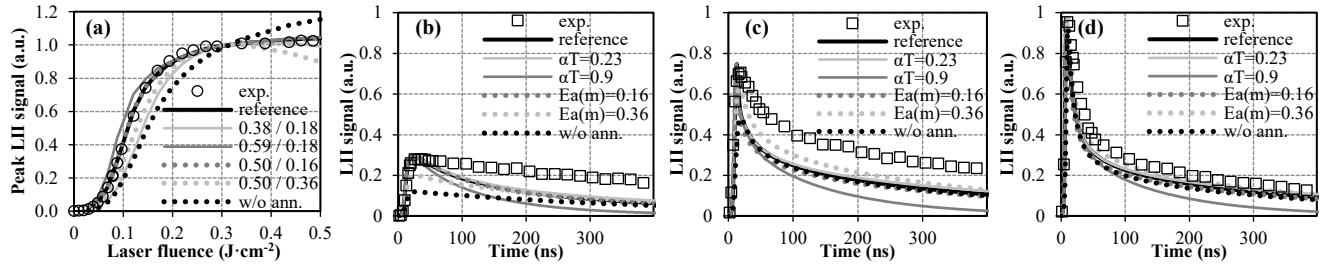

Fig. 3: Comparison between measured (exp.) and simulated LII fluence curves (a) and time decays ((b), (c) and (d)). Calculations are performed with model 3. Black lines denoted as 'reference' are issued from simulations carried out using the following parameters: $E(m)$=0.50, $E_a(m)$=0.18 and α_T=0.3. The pairs 'x/y' in (a) stand for tested $E(m)$ and $E_a(m)$. Time decays in (b) to (d) are obtained with fluences of: (b) 0.09 J.cm^{-2}, (c) 0.15 J.cm^{-2} and (d) 0.27 J.cm^{-2}. The parameters specified in the legends of (b) to (d) are those whose values are modified with respect to the reference case.

Results depicted in **Fig. 3(a)** show that calculations performed when setting the value of $E(m)$ to 0.50 while keeping a $E_a(m)$ of 0.18, as suggested in [**8**], leads to a good agreement between measured and simulated fluence curves (see the black curve denoted as 'reference' in **Fig. 3(a)**). Contrary to models 1 and 2 which failed to reproduce a lack of fluence dependence of LII signals above the sublimation threshold, model 3 is able, when properly parameterized, to simulate the evolution of the peak LII signals for fluences up to 0.5 J·cm^{-2}. **Fig. 3(a)**, moreover, shows that for a given $E(m)$, increasing the $E_a(m)$ from 0.16 to 0.36 has a major impact on the modeling of the peak intensity of LII signals in the high fluence regime, thus corroborating the relevance of considering soot annealing in LII modeling. While theoretical time decays globally match measured ones at high fluences (see **Fig. 3(d)**), diverging trends are still observed below the sublimation threshold (see **Figs. 3(b)** and **3(c)**). Here again, and as previously exemplified in **Fig. 2**, adjusting the α_T from 0.23 to 0.9 has only a limited impact on the agreement between measured and predicted signals. Conversely, embedding the annealing flux within the model formulation allows predicting time decays that better fit experimentally monitored ones (which is consistent with the better simulation of the fluence curves, as shown in **Fig. 3(a)**). As such, and despite the discrepancies highlighted in **Figs. 3(b)** and **3(c)**, the predictive ability of model 3 is shown to be better than that of models 1 and 2, which can be notably attributed to the rate of energy increase by annealing that proved to significantly influence the LII process, especially at high fluences. The fact that obtaining a good agreement between measured and simulated fluence curves implies setting a relatively high $E(m)$ (0.50), however, prompts the need for further analyses aimed at properly parameterizing model 3 so as to complement this preliminary analysis.

Concerning model 4, we first led a sensitivity analysis focusing on some parameters influencing the absorption and sublimation terms (see **Fig. 4**), including $E(m)$, $B_{\lambda 1}$, $B_{\lambda n}$ and $\sigma_{\lambda n}$ (see Eq. (5)), as well as $\Delta H_{\lambda n,s}$ (see Eq. (9)). To that end, and although being initially proposed for an excitation wavelength of 532 nm, the parameters from [**4**] were used as reference ones since no other parameter sets have been proposed in the literature for a 1064-nm excitation wavelength (except in [**10**],

as discussed below). Furthermore, it should be noted that the aim of this preliminary sensitivity analysis is solely to assess the relative impact of the above-listed parameters and not to define optimal ones.
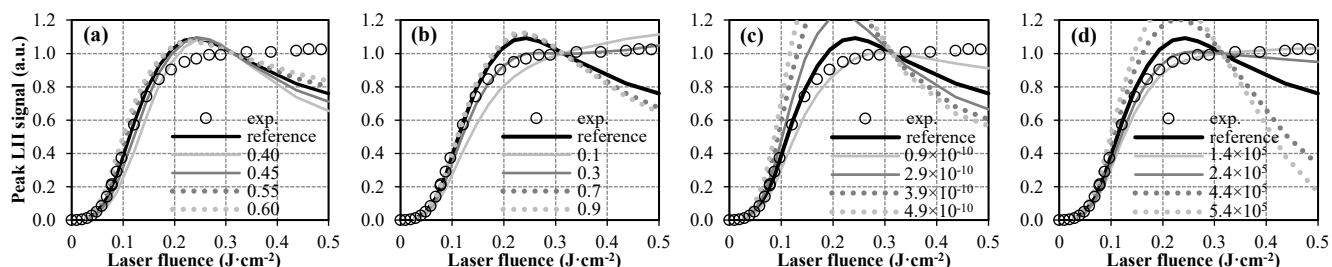

Fig. 4: Comparison of measured (exp.) LII fluence curves with simulated ones issued from the implementation of model 4 integrating the thermionic sub-model from [**4**]. Black lines denoted as 'reference' are issued from simulations carried out using the following parameters: $E(m)$=0.50, $B_{\lambda 1}$=0.6 J.cm^{-2}, $B_{\lambda n}$=0.5 J.cm^{-2}, $\sigma_{\lambda n}$=1.9×10^{-10} cm^{2n-1}·J^{1-n}, $\Delta H_{\lambda n,s}$=3.4×10^5 J.mol^{-1} and α_T=0.3. Calculations made with varied $E(m)$, $B_{\lambda n}$, $\sigma_{\lambda n}$ and $\Delta H_{\lambda n,s}$ values are depicted in (a), (b), (c) and (d), respectively.

While the expression of $\dot{Q}_{th}$ and the value taken by $B_{\lambda 1}$ have a relatively limited impact on the agreement between measured and modeled fluence curves for fluences up to 0.3 J·cm^{-2} (thus explaining why corresponding results are not reported in **Fig. 4**, for brevity), adjusting the $E(m)$ value can significantly improve the predictive character of model 4 in the low-to-intermediate fluence regime. None of the tested $E(m)$ truly allows mimicking experimental results for fluences above 0.2 J·cm^{-2}, however. As for $B_{\lambda n}$ and $\Delta H_{\lambda n,s}$, selecting values of around 0.3 J.cm^{-2} and 1.4×10^5 J.mol^{-1}, respectively, clearly allows reproducing the fluence dependence of the LII signals up to 0.5 J·cm^{-2} (see **Figs. 4(b)** and **4(d)**), noting that modifying the $\sigma_{\lambda n}$ value also drastically impacts computed fluence curves. These results thus tend to corroborate the conclusions drawn in [**7**] regarding the importance of integrating photolytic mechanisms such as multi-photon absorption and nonthermal photodesorption of carbon clusters to simulate soot LII over an extended range of operating conditions. Although using a different model formulation that includes annealing in addition to mechanisms representing multiple scattering within aggregates, [**10**] recently proposed optimized values for the above-listed parameters when considering a 1064-nm excitation wavelength. By considering these values together with an $E(m)$ of 0.5, as estimated based on **Fig. 4(a)**, one obtains the results depicted in **Fig. 5**.
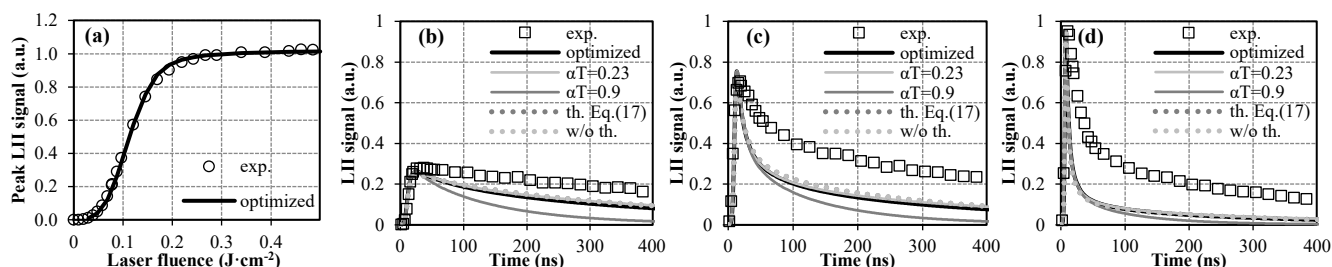

Fig. 5: Comparison of measured (exp.) and simulated (model 4) LII fluence curves (a) and time decays ((b), (c) and (d)). Optimized results (black lines) are obtained using Eq. (16) together with the following parameters: $E(m)$=0.50, $B_{\lambda 1}$=1.15 J.cm^{-2}, $B_{\lambda n}$=0.41 J.cm^{-2}, $\sigma_{\lambda n}$=4.2×10^{-10} cm^{2n-1}·J^{1-n}, $\Delta H_{\lambda n,s}$=1.7×10^5 J.mol^{-1} and α_T=0.3. Time decays are plotted for fluences of (b) 0.09 J.cm^{-2}, (c) 0.15 J.cm^{-2} and (d) 0.27 J.cm^{-2} and parameters which have been modified with respect to the reference case are specified in the legends.

An excellent agreement can be observed between measured and simulated fluence curves (see **Fig. 5(a)**), which may be related to the inclusion and correct parameterization of the terms accounting for the multi-photon absorption process leading to the photodesorption of C_2 clusters. On the other hand, and as can be seen by looking at **Fig. 5(b)** to **5(d)**, model 4 fails to properly reproduce measured LII time decays, regardless of the selected α_T value, thus prompting the need for additional optimization work for the specific model formulation tested herein.

4. Conclusion

The predictive ability of 4 LII models from the literature was assessed against data obtained in an ethylene diffusion flame using a 1064-nm laser excitation source [5]. As highlights, this work in progress showed that standard model formulations can satisfactorily reproduce peak soot temperature profiles as well as LII fluence curves for fluences below J·cm^{-2}. The models, as they were parameterized in this study, however, failed to properly simulate LII time decays, which would prevent them from being used to satisfactorily estimate soot size by time-resolved LII, for instance. As for refined models, the sensitivity analyses proposed herein showed that annealing, multi-photon absorption and nonthermal photodesorption of carbon clusters are important processes likely to better capture the physics at play during high-fluence LII measurements. That being said, and although exhibiting better predictive capabilities (especially in the case of model 3) as compared to more simplified simulation tools, none of the tested models allowed reproducing LII fluence curves and time decays over an extended range of operating conditions. Complementary works based on the use of other experimental datasets would therefore be of interest to distinguish whether the observed discrepancies are due to the experiments specifically or are due to the models, thus paving the way for future works to be undertaken.

References

[1] H. Michelsen, C. Schulz, G.J. Smallwood, S. Will, "Laser-induced incandescence: Particle diagnostics for combustion, atmospheric, and industrial applications," *Prog. Energy Combust. Sci.*, vol. 51, pp. 2-48, 2015.

[2] Z. Zhang, L. Zhou, X. He, "Can laser-induced incandescence calibrated by laser extinction method be used for quantitative determination of soot volume fraction in laminar flames?", *Appl. Energy, Combust. Sci.*, vol 13, pp. 100103, 2023.

[3] L. A. Melton, "Soot diagnostics based on laser heating," *Appl. Opt.*, vol. 23, pp. 2201-2208, 1984.

[4] H. A. Michelsen, F. Liu, B. F. Kock, H. Bladh, A. Boiarciuc, M. Charwath, T. Dreier, R. Hadef, M. Hofmann, J. Reimann, S. Will, P. -E. Bengtsson, H. Bockhorn, F. Foucher, K. -P. Geigle, C. Mounaïm-Rousselle, C. Schulz, R. Stirn, B. Tribalet, R. Suntz, "Modeling laser-induced incandescence of soot: a summary and comparison of LII models," *Appl. Phys. B*, vol. 87, pp. 503-521, 2007.

[5] F. Goulay, P. E. Schrader, X. López-Yglesias, H. A. Michelsen, "A data set for validation of models of laser-induced incandescence from soot: temporal profiles of LII signal and particle temperature," *Appl. Phys. B*, vol. 112, pp. 287-306, 2013.

[6] M. Hofmann, B. Kock, C. Schulz, "A web-based interface for modeling laser-induced incandescence (LIISim)," in *Proceedings of the Third European combustion meeting*, Chania, Greece, <http://www.LIIsim.com>, 2007.

[7] R. Lemaire, M. Mobtil, "Modeling laser-induced incandescence of soot: a new approach based on the use of inverse techniques," *Appl. Phys. B*, vol. 119, pp. 577-606, 2015.

[8] H. A. Michelsen, "Understanding and predicting the temporal response of laser-induced incandescence from carbonaceous particles," *J. Chemical Phys.*, vol. 118, pp. 7012-7045, 2003.

[9] G.J. Smallwood, D. Snelling, F. Liu, Ö.L. Gülder, "Clouds over soot evaporation: errors in modeling laser-induced incandescence of soot," *J. Heat Transfer*, vol. 123, pp. 814-818, 2001.

[10] R. Lemaire, S. Menanteau, "Modeling laser-induced incandescence of Diesel soot—Implementation of an advanced parameterization procedure applied to a refined LII model accounting for shielding effect and multiple scattering within aggregates for α_T and E(m) assessment," *Appl. Phys. B*, vol. 138, pp. 1-19, 2021.

[11] J.M. Mitrani, M.N. Shneider, B.C. Stratton, Y. Raitses, "Modeling thermionic emission from laser-heated nanoparticles," *Appl. Phys. Lett.*, vol. 108, pp. 054101, 2016.